Polarization rotator-splitter covering full optical communication bands based on L-shaped cross-section waveguide

Daigao Chen (陈代高)[1,2], Xi Xiao (肖 希)[2,*], Lei Wang (王 磊)[2], Wen Liu (刘 文)[1,3,], and Qi Yang (杨 奇)[2]**

[1]*Wuhan National Laboratory for Optoelectronics, Huazhong University of Science and Technology, Wuhan 430074, China*

[2]*State Key Laboratory of Optical Communication Technologies and Networks, Wuhan Research Institute of Posts Telecommunications, Wuhan 430074, China*

[3]*Department of Optics and Optical Engineering, University of Science and Technology of China, Hefei 230026, China*

**Corresponding author: xxiao@wri.com.cn; **corresponding author: liuwen.316@163.com*

Received December 9, 2015; accepted January 25, 2016; posted online March 22, 2016

We propose an ultra-broadband and fabrication-tolerant polarization rotator-splitter (PRS) based on a waveguide with an L-shaped cross section and a Y-junction. The proposed PRS is based on the 220 nm silicon-on-insulator platform, and it shows less than 0.27 dB insertion losses and larger than 14 dB polarization extinction ratios over a wavelength range from 1200 to 1700 nm. To the best of our knowledge, the PRS working in the whole optical communication band is proposed for the first time.

OCIS codes: 130.3120, 130.5440, 230.7370.

doi: 10.3788/COL201614.041301.

Benefited by their high index contrast and compatibility with commercial complementary metal oxide semiconductor (CMOS) processes, silicon photonics has become a promising technology for low-cost and high-performance optical communications[1]. Silicon optical devices have recently attracted more and more attention[2–4]. However, the structural asymmetry of the submicron-scale silicon waveguide induces a large polarization birefringence. A polarization rotator-splitter (PRS) is an indispensable device for polarization division multiplexing in coherent optical communications. Recently, an on-chip silicon PRS was demonstrated mostly by using the following methods: integrating a separate polarization rotator (PR) with a polarization splitter[5–7], designing an asymmetrical directional coupler to rotate and split the polarization simultaneously[8–10], and combining mode evolution devices with mode sorting devices based on the TE_1 mode transition[11–16]. According to the reported works, the PRS based on the third method shows the largest bandwidth[14].

For the third method, a slowly varying T-shaped cross section waveguide[12–15] or an equivalent structure (T-waveguide)[11,16] is used to convert the TM_0 mode to the TE_1 mode, while the input TE_0 maintains its polarization. Then, a mode order converter and splitter are connected to the end of the T-waveguide to split the TE_1 and TE_0 modes and convert the TE_1 mode to the TE_0 mode at the same time (mode sorting). According to Ref. [17], mode conversion happens when there is a mode hybridization of the two modes. So the key for realizing TE_1-based PRS is a waveguide structure where its TE_1 and TM_0 modes are hybridized. So far, the slowly varying T-waveguide is the only method to convert the TM_0 mode to the TE_1 mode efficiently. Besides, although a PRS consisting of an asymmetrical Y-junction (used as a mode sorter) and a T-waveguide shows the largest bandwidth[14], a high-resolution lithography process is necessary for the tip of Y-junction, because a sharp tip is crucial for highly efficiency mode sorting[14,18–20].

The L-shaped cross-section waveguide (L-waveguide), which consists of waveguides with different heights, has been used as a PR between fundamental modes[21,22]. But using an L-waveguide for higher-order modes has not been reported, due to the irregular mode field distribution in this kind of waveguide. However, in this work, we propose a novel PRS based on a TE_1-like mode in an L-waveguide for the first time. An asymmetrical Y-junction with two branches of different heights is used for mode sorting. The sharp tip is realized by overlay lithography between two layers. Thus, high-resolution lithography is not needed. Otherwise, both of the two waveguides are used to guide the mode, as this increases the design dimensions. The designed PRS based on a silicon-on-insulator (SOI) wafer with a 220 nm Si layer shows insertion losses (ILs) of less than 0.27 dB, and polarization extinction ratios (ERs) of more than 14 dB over a wavelength range from 1200 to 1700 nm. Besides, this kind of PRS has a high fabrication tolerance. To the best of our knowledge, it is the first PRS that can work over all optical communication bands (the wavelength range from 1260 to 1675 nm).

The design is based on an SOI wafer with the 220 nm-thick silicon covered by an SiO_2 upper cladding

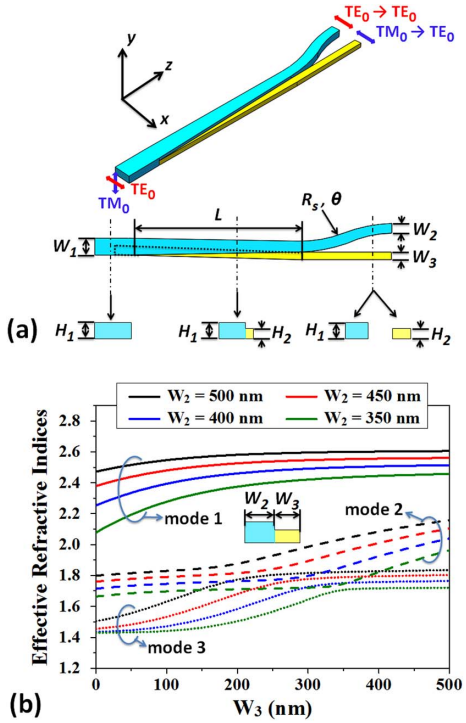

Fig. 1. (a) Schematic of the proposed PRS. Top: three-dimensional view, middle: overhead view, and bottom: cross-section view. The dotted lines encircling the region are the overlap of the two different waveguides. (b) The effective refractive indices of the first three modes of the L-waveguide as the function of the higher waveguide width (W_2) and the lower waveguide width (W_3). The calculation wavelength is 1550 nm. Mode 1, mode 2, and mode 3 are represented by the solid, dashed, and dotted lines, respectively.

($n_{\mathrm{Si}} = 3.47$, and $n_{\mathrm{SiO_2}} = 1.444$ at the wavelength of 1550 nm). The schematic of the PRS is shown in Fig. 1(a), and consists of two partially overlapping waveguides with different heights. The height of the higher waveguide H_1 is 220 nm, and that of the lower waveguide H_2 is 150 nm. The dotted lines in the overhead view indicate the overlap of the two waveguides. This can help one to avoid needing high-resolution lithography and reduces the decline of the mode sorting efficiency caused by the alignment error during the lithography. The length of the L-waveguide is labeled L. The higher waveguide is symmetrically tapered from W_1 (fixed at 500 nm) to W_2 along L. The non-overlapped part of the lower waveguide is tapered from 0 nm to W_3 along L. An asymmetrical Y-junction composed of an S-bend waveguide (higher waveguide with the width W_2) and a straight waveguide (lower waveguide with the width W_3) connects to the L-waveguide. The radius of the S-bend waveguide is R_s, and the bending angle is θ. The proposed device can be fabricated by the following process. First, a hard mask is deposited on the Si layer, and the pattern of the higher waveguide is transferred to the hard mask. Second, the region where there is no pattern is etched to a height of 150 nm. Third, the photoresist is deposited, and the pattern of the lower waveguide (including the region surrounded by the dotted line) is transferred to the photoresist. Fourth, the region where there is no pattern is etched through (it should be noted that the hard mask pattern still exists in this step). Finally, a 3 μm-thick SiO_2 layer is deposited.

The three-dimensional finite-difference time-domain method is implemented to simulate the structure. To choose a reasonable output waveguide width, we calculate the effective refractive indices (n_{eff}) of the first three modes of the L-waveguide at 1550 nm. We set $W_2 = 500$, 450, 400, and 350 nm, and sweep the value of W_3 from 0 to 500 nm for each W_2 correspondingly. The result is shown in Fig. 1(b). It can be seen that the mode hybridization region appears at $W_3 = 180$–350 nm for all of the four W_2 settings. In this work, we set $W_2 = 450$ and $W_3 = 400$ nm for the output waveguide to guarantee that there is a mode hybridization region in the L-waveguide. Such a width combination also meets the mode sorting principle of the asymmetrical Y-junction[14,18], that is $|n_{\mathrm{eff}}^{\mathrm{stem,TE_1}} - n_{\mathrm{eff}}^{W_3,\mathrm{TE_0}}| < |n_{\mathrm{eff}}^{\mathrm{stem,TE_1}} - n_{\mathrm{eff}}^{W_2,\mathrm{TM_0}}|$, where $n_{\mathrm{eff}}^{\mathrm{stem,TE_1}}$ is the n_{eff} of the $\mathrm{TE_1}$-like mode in the right end of the L-waveguide, $n_{\mathrm{eff}}^{W_3,\mathrm{TE_0}}$ is the n_{eff} of the $\mathrm{TE_0}$ mode in the lower waveguide of the Y-junction, and $n_{\mathrm{eff}}^{W_2,\mathrm{TM_0}}$ is the n_{eff} of the $\mathrm{TM_0}$ mode in the higher waveguide of the Y-junction.

Figure 2(a) shows the mode and the mode's indices evolution along the L-waveguide with $W_2 = 450$ and $W_3 = 400$ nm at the wavelength of 1550 nm. It can be

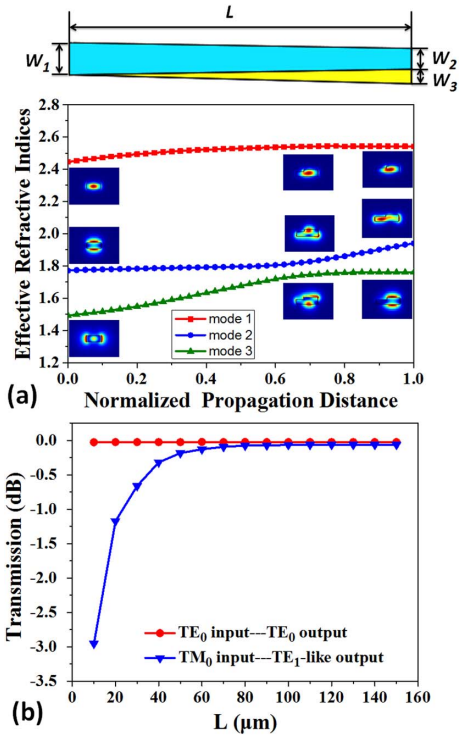

Fig. 2. (a) Mode indices and profiles evolution along the L-waveguide with $W_2 = 450$ and $W_3 = 400$ nm at the wavelength of 1550 nm. (b) Average transmission efficiency varied with the L-waveguide length over a wavelength range from 1500 to 1600 nm.

seen that the mode hybridization happens at $\approx 0.64L$. The inset clearly shows the mode evolution along the propagation direction. In the beginning ($W_1 = 500$ nm), the mode 1, mode 2, and mode 3 are TE_0, TM_0, and TE_1 mode, respectively. While at the end ($W_2 = 450$ and $W_3 = 400$ nm), the mode 1, mode 2, and mode 3 are TE_0, TE_1-like and TM_0 mode, respectively. Then we sweep the L-waveguide length L for a sufficient conversion between the TM_0 mode and the TE_1-like mode over a wavelength range from 1500 to 1600 nm. As shown in Fig. 2(b), when L is larger than 70 μm, the average transmission efficiencies of both polarization inputs are more than −0.1 dB (97.7%). When $L = 110$ μm, the average conversion efficiency of the TM_0 mode to the TE_1-like mode reaches its maximum, −0.064 dB (98.5%). Thus, in the following calculation, L is fixed at 110 μm.

According to Refs. [18–20], if the mode conversion factor (MCF) is larger than 0.43, the asymmetrical Y-junction can be used as a mode sorter. The MCF is inversely proportional to the angle (φ) between the Y-junction arms. φ varies with bending radiuses of the S-bend waveguide in the asymmetrical Y-junction. For high-efficiency mode sorting and to avoid bending loss, we sweep the radius starting with 30 μm with θ fixed at 15°, as shown in Fig. 3. It can be seen that the average transmission efficiency variation of the input TE_0 mode is the same as that of the converted TE_0 mode from the TE_1-like mode. Both of them are more than 98.8% (−0.05 dB loss) when $R_s = 35$ μm.

Then the total transmission efficiency is calculated when connecting the optimized asymmetrical Y-junction with the L-waveguide. The above device has a total length of about 127 μm. Initially, to save time in the simulation, only the efficiency over a wavelength range from 1500 to 1600 nm is calculated. For analyzing the bandwidth property of this PRS, the simulation is implemented at a wavelength range from 1200 to 1700 nm, which covers the entire optical communication band (from 1260 to

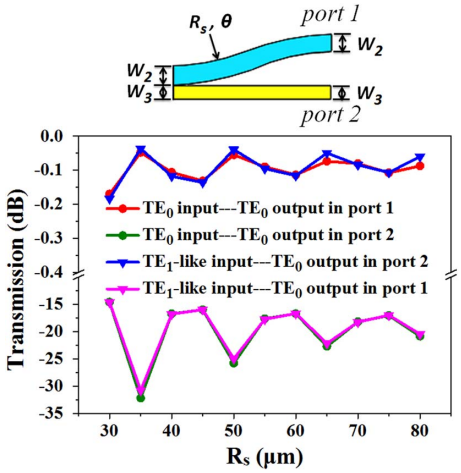

Fig. 3. Average transmission efficiency varied with the radius of the S-bend waveguide of the asymmetrical Y-junction over a wavelength range from 1500 to 1600 nm.

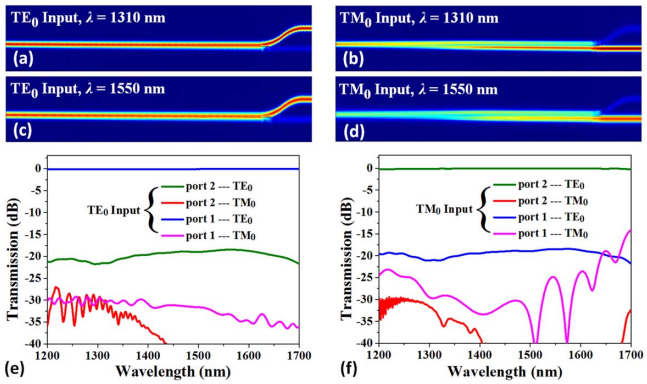

Fig. 4. (a)–(d) Simulated field intensity distributions at 1310 and 1550 nm wavelengths. (e)–(f) Different modes' outputs efficiencies as a function of the wavelength in the two output ports. Transmission efficiency below −40 dB is not shown.

1675 nm). The simulation results are shown in Fig. 4. Over the simulation wavelength range, the ILs and the ERs of both polarization inputs are less than 0.25 dB and more than 14 dB, respectively.

The length of the proposed PRS is also optimized for a smaller footprint. In fact, the L-waveguide can be divided into three parts. The long beginning and ending parts of the L-waveguide have limited contributions to the polarization conversion. Those parts act as mode size converters more than polarization converters. The polarization conversion primarily occurs in the middle part. For the mode size converter, the lengths of the beginning and ending parts are still too long. To shorten those parts and design a more compact device, as shown in Fig. 5(a), we set the exposed middle part of the lower waveguide tapering from $W_{11} = 180$ to $W_{22} = 350$ nm, and the corresponding higher waveguide tapering from $W_{33} = 478$ to W_{44}=456nm. Then the length of this part is $L_1 = (W_{22} - W_{11})L/W_3 \approx 47$ μm, and the length of the beginning and ending parts are shortened to $L_2 = L_3 = 10$ μm; thus, the total length of the short PRS is about 84 μm.

The simulation results of the shortened PRS are shown in Fig. 5. Over the simulation wavelength range, the ILs and the ERs of both polarization inputs are less than 0.27 dB and more than 14 dB, respectively. By comparing Figs. 4(f)–5(h), it can been seen that the output of the TM_0 mode in port1 of the short PRS is higher than that of the long PRS at some wavelengths, which means the polarization conversion in the short PRS is not sufficient as that in the long PRS. However, the remaining TM_0 modes of both PRSs are less than −14 dB (4%), indicating that the polarization conversions in the beginning and ending parts of the both PRSs are somewhat acceptable for most applications.

To investigate the fabrication tolerance of the PRS, we simulate the transmission efficiency variations with the width deviations of the waveguides, the alignment error of the two waveguides heights, and the etching depth deviation at 1310 and 1550 nm. Considering the practical process conditions, we set the width deviation within

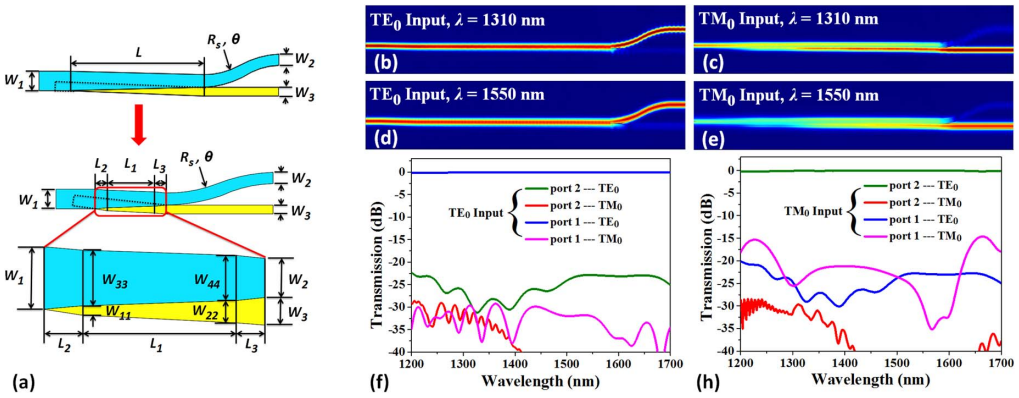

Fig. 5. (a) Schematic of the proposed PRS. Top: before shortening, bottom: after shortening. (b)–(e) Simulated field intensity distributions of the shortened PRS at 1310 and 1550 nm wavelengths. (f)–(h) Different modes' output efficiencies as a function of the wavelength in the two output ports of the shortened PRS. Transmission efficiencies below −40 dB are not shown.

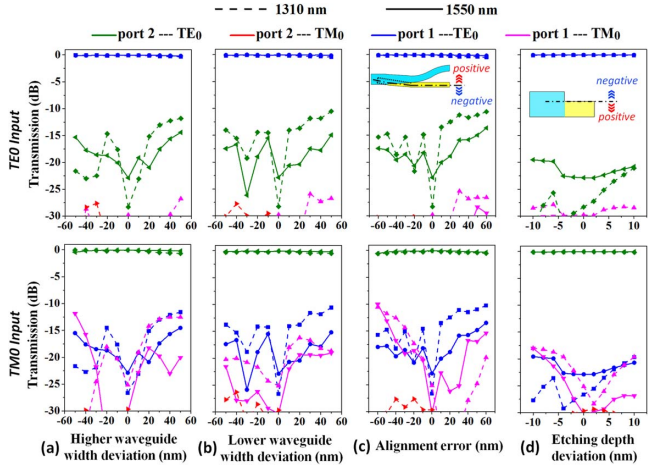

Fig. 6. Simulated the transmission efficiencies varied with (a) the higher waveguide width deviation, (b) the lower waveguide width deviation, (c) the alignment error, and (d) the etching depth deviation. The transmission efficiencies of 1310 nm wavelength are the dashed line, and that of the 1550 nm wavelength are the solid line. The above figures are the TE_0 input situation, and the bottom figures are the TM_0 input situation. The inset in figure (c) demonstrates the alignment error, and the dashed–dotted line is the center line of the lower waveguide. The inset in figure (d) demonstrates the etching depth deviation, and the dashed–dotted line is the upper surface of the lower waveguide. Transmission efficiencies below −30 dB are not shown.

50 nm, the alignment error within 60 nm, and the etching depth deviation within 10 nm. As shown in Figs. 6(a)–6(c), the IL deviations with the fabrication errors are small. The worst IL, when the TM_0 mode input and the width of the higher waveguide is widened by 50 nm, is still less than 0.69 dB. The polarization ER has serious deviations with the waveguide dimension variations and the alignment errors. But the worst ER, when the TM_0 mode input and the alignment error is −60 nm, is still about 10 dB, as shown in the bottom of Fig. 6(c). From Fig. 6(d), it can be seen that the etching depth deviation has little effect on the ILs and polarization ERs. In general, the PRS is highly fabrication tolerable.

Table 1. Comparison of the PRSs With Bandwidths Greater Than 300 nm

Structure	Directional coupler [10]	T-waveguide and asymmetrical Y-junction [14]	L-waveguide and asymmetrical Y-junction (our device)
IL	N/A	0.4 dB	0.27 dB
ER	25 dB	12 dB	14 dB
Bandwidth	300 nm	400 nm	500 nm
Length	400 μm	95 μm	84 μm
Min linewidth	150 nm (gap)	0 nm (tip)	400 nm
Cladding	Si_3N_4	SiO_2	SiO_2

Table 1 compares our device with the reported PRSs whose bandwidths are more than 300 nm. It can be seen our PRS has the most compact size, the broadest bandwidth, and needs the lowest lithography resolution.

In conclusion, we propose a novel L-waveguide-based PRS covering the whole optical communication band. The L-waveguide is designed for the mode evolution and an asymmetric Y-junction is used for the mode sorting. The PRS shows ILs of less than 0.27 dB and polarization ERs of above 14 dB over a wavelength range from 1200 to 1700 nm. The proposed PRS has a high fabrication tolerance and is ready for CMOS fabrication. This device can be a universal solution to the silicon optical device's polarization diversity for the applications of datacom, metro, and long-haul optical communications.

References

1. M. Hochberg and T. Baehr-Jones, Nat. Photon. **4**, 492 (2010).

2. J. Xing, Z. Li, P. Zhou, Y. Gong, Y. Yu, M. Tan, and J. Yu, Chin. Opt. Lett. **13**, 061301 (2015).
3. J. Zhang, J. Yang, H. Lu, W. Wu, J. Huang, and S. Chang, Chin. Opt. Lett. **13**, 091301 (2015).
4. X. Zhao, Y. Zhang, C. Zeng, D. Li, G. Gao, Q. Huang, Y. Wang, J. Yu, and J. Xia, Chin. Opt. Lett. **13**, 101301 (2015).
5. L. Chen, C. R. Doerr, and Y. K. Chen, Opt. Lett. **36**, 469 (2011).
6. A. Xie, L. Zhou, J. Chen, and X. Li, Opt. Express **23**, 3960 (2015).
7. H. Fukuda, K. Yamada, T. Tsuchizawa, T. Watanabe, H. Shinojima, and S. Itabashi, Opt. Express **16**, 4872 (2008).
8. H. Guan, A. Novack, M. Streshinsky, R. Shi, Q. Fang, A. E. J. Lim, G. Q. Lo, T. Baehr-Jones, and M. Hochberg, Opt. Express **22**, 2489 (2014).
9. Y. Xiong, J. G. Wangüemert-Pérez, D. X. Xu, J. H. Schmid, P. Cheben, and W. N. Ye, Opt. Lett. **39**, 6931 (2014).
10. L. Socci, V. Sorianello, and M. Romagnoli, Opt. Express **23**, 19261 (2015).
11. D. Dai and J. E. Bowers, Opt. Express **19**, 10940 (2011).
12. H. Guan, A. Novack, M. Streshinsky, R. Shi, Y. Liu, Q. Fang, A. E. J. Lim, G. Q. Lo, T. B. Jones, and M. Hochberg, IEEE Photon. Technol. Lett. **26**, 925 (2014).
13. W. D. Sacher, Y. Huang, L. Ding, T. Barwicz, J. C. Mikkelsen, B. J. F. Taylor, G. Q. Lo, and J. K. S. Poon, Opt. Express **22**, 11167 (2014).
14. J. Wang, B. Niu, Z. Sheng, A. Wu, W. Li, X. Wang, S. Zou, M. Qi, and F. Gan, Opt. Express **22**, 13565 (2014).
15. J. Wang, M. Qi, Y. Xuan, H. Huang, Y. Li, M. Li, X. Chen, Q. Jia, Z. Sheng, A. Wu, W. Li, X. Wang, S. Zou, and F. Gan, Opt. Express **22**, 27869 (2014).
16. Y. Ding, H. Ou, and C. Peucheret, Opt. Lett. **38**, 1227 (2013).
17. D. Dai, Y. Tang, and J. E. Bowers, Opt. Express **20**, 13425 (2012).
18. N. Riesen and J. D. Love, Appl. Opt. **51**, 2778 (2012).
19. J. B. Driscoll, R. R. Grote, B. Souhan, J. I. Dadap, M. Lu, and R. M. Osgood, Opt. Lett. **38**, 1854 (2013).
20. W. Chen, P. Wang, and J. Yang, IEEE Photon. Technol. Lett. **26**, 2043 (2014).
21. M. Aamer, A. M. Gutierrez, A. Brimont, D. Vermeulen, G. Roelkens, J. M. Fedeli, A. Håkansson, and P. Sanchis, IEEE Photon. Technol. Lett. **24**, 2031 (2012).
22. K. Goi, A. Oka, H. Kusaka, K. Ogawa, T. Y. Liow, X. Tu, G. Q. Lo, and D. L. Kwong, Opt. Lett. **40**, 1410 (2015).